Article

Mesoporous Nano-Badminton with Asymmetric Mass Distribution: How Nanoscale Architecture Affects the Blood Flow Dynamics

Tiancong Zhao, Runfeng Lin, Borui Xu, Minchao Liu, Liang Chen, Fan Zhang, Yongfeng Mei, Xiaomin Li,* and Dongyuan Zhao*

Read Online

ACCESS | Metrics & More | Article Recommendations | Supporting Information

ABSTRACT: While the nanobio interaction is crucial in determining nanoparticles' in vivo fate, a previous work on investigating nanoparticles' interaction with biological barriers is mainly carried out in a static state. Nanoparticles' fluid dynamics that share non-negligible impacts on their frequency of encountering biological hosts, however, is seldom given attention. Herein, inspired by badmintons' unique aerodynamics, badminton architecture Fe_3O_4&mPDA (Fe_3O_4 = magnetite nanoparticle and mPDA = mesoporous polydopamine) Janus nanoparticles have successfully been synthesized based on a steric-induced anisotropic assembly strategy. Due to the "head" Fe_3O_4 having much larger density than the mPDA "cone", it shows an asymmetric mass distribution, analogous to real badminton. Computational simulations show that nanobadmintons have a stable fluid posture of mPDA cone facing forward, which is opposite to that for the real badminton. The force analysis demonstrates that the badminton-like morphology and mass distribution endow the nanoparticles with a balanced motion around this posture, making its movement in fluid stable. Compared to conventional spherical Fe_3O_4@mPDA nanoparticles, the Janus nanoparticles with an asymmetric mass distribution have straighter blood flow trails and ~50% reduced blood vessel wall encountering frequency, thus providing doubled blood half-life and ~15% lower organ uptakes. This work provides novel methodology for the fabrication of unique nanomaterials, and the correlations between nanoparticle architectures, biofluid dynamics, organ uptake, and blood circulation time are successfully established, providing essential guidance for designing future nanocarriers.

■ INTRODUCTION

The development of nanotechnology has promoted remarkable advances in the treatment of diseases.[1−7] Nanoparticles' interactions with biological interfaces (cells, vessels, and organs) have profound effects on their in vivo blood circulation time, organ uptake, etc., and a huge amount of work has been done to investigate the nanobio interactions.[8−15] However, while previous works have demonstrated that the physicochemical properties of nanoparticles (size,[16−18] shape,[19−21] surface chemistry,[22−24] density[25] etc.) have major effects on these interactions, most of the research studies were done based on the assumption that nanoparticles have already encountered with the biological interfaces. These studies about nanobio interactions are controversial from a real in vivo motion state.[26]

Upon nanoparticles' intravenous injection, the nanoparticles are constantly in passive movements in the flowing bloodstream,[17,23,27] which have velocities varying from 10 cm s^{-1} in artery[28] to 10 μm s^{-1} in capillary/sinusoids.[29] Some researchers have been interested in how nanoparticle motion affects their margination on vessels and have investigated how flow velocity changes nanoparticle-vessel/cell interactions. Some researchers have studied the role of nanoparticle morphology and have investigated the effect of morphology (e.g., shuttle/spherical) on the relevant behaviors.[30,31] Never-

theless, limited by the complexity of nanoparticle morphology modulation, related research has been a major challenge in the field of nanomedicine. Therefore, it is urgently desired to study on the correlations among nanoparticle's architectures, biofluid dynamics, blood circulation, and organ accumulation.[32−36]

On the macroscopic scale, the fluid dynamics of objects are highly dependent on their architectures. For example, badminton with cone shape and asymmetric mass distribution provides a unique aerodynamic with stable and straight movement trails.[37,38] It naturally makes one feel interested in whether the architecture and dynamic relationship of badmintons still works at the nanoscale. We hypothesize that a badminton-like nanoparticle can move linearly just like real badmintons. However, though many kinds of anisotropic nanoparticles have been reported,[20,39−42] nanoparticles with such a badminton-like architecture are yet to be fabricated.

Herein, inspired by the badmintons' architecture-induced stable aerodynamics, based on the steric-induced anisotropic
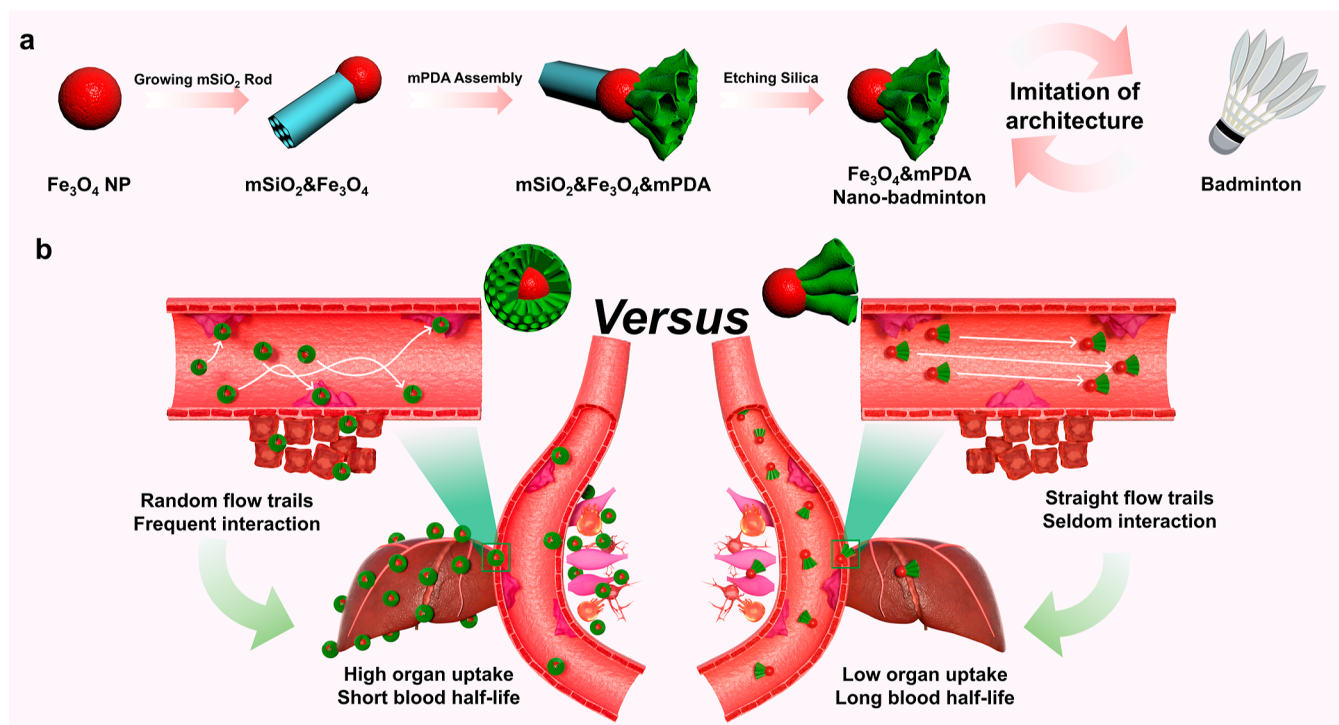
Figure 1. Synthesis and unique flow dynamics of nanobadmintons. (a) Schematic illustration of the synthesis of the Fe_3O_4&mPDA nanobadmintons with asymmetric mass distribution. (b) Schematic illustration of the nanobadmintons' unique blood flow dynamics comparing to conventional nanospheres, which brings straighter flowing trails, decreased encountering frequency with vascular walls, and thereupon lower organ uptake and lengthen blood circulation time.
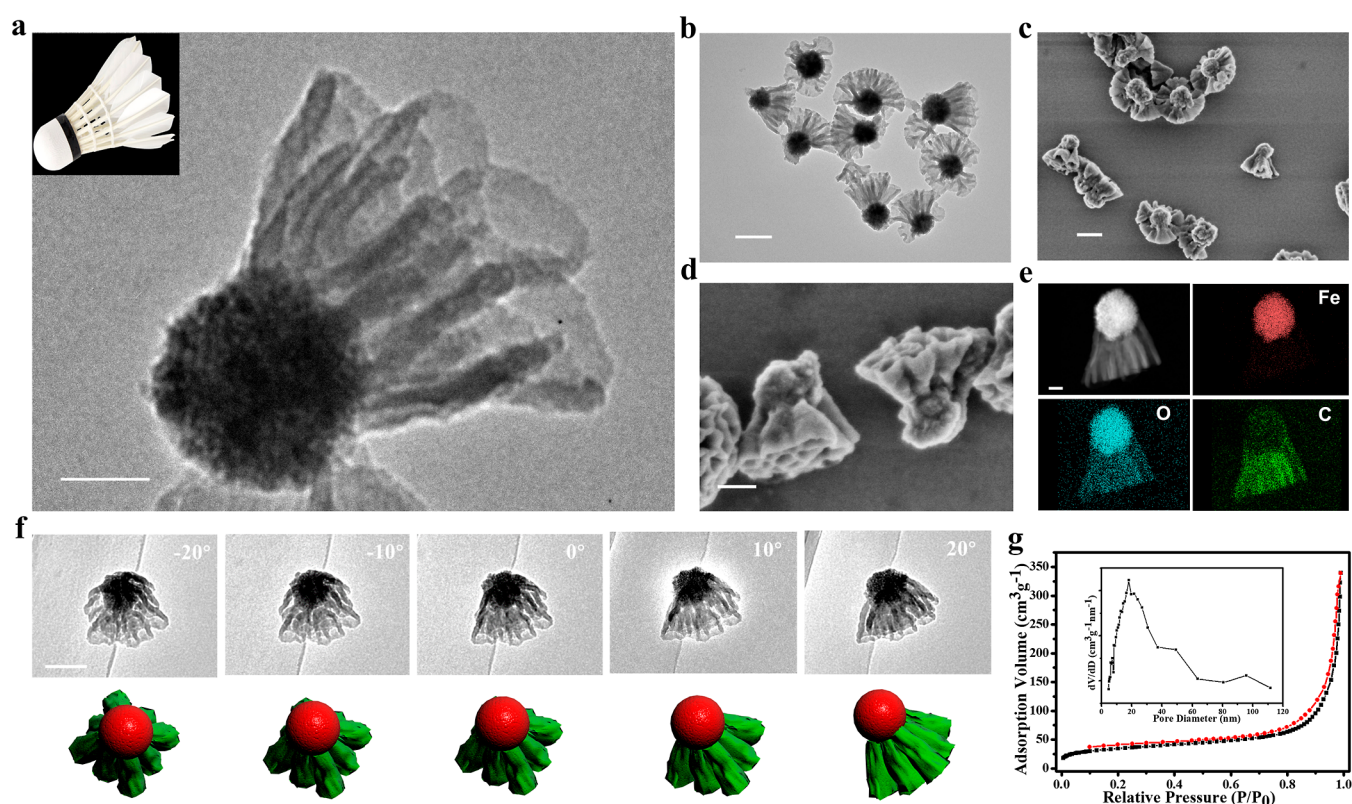
Figure 2. Synthesis and characterization of nanobadmintons. (a–d) TEM and SEM images with different magnifications and (e) elemental mapping of the badminton-like Fe_3O_4&mPDA nanoparticles. (f) In situ tilting observations, 3D models and (g) nitrogen sorption isotherms of the badminton-like Fe_3O_4&mPDA nanoparticles. The inset of (a) is a photo of a badminton. The inset of (g) is the pore size distribution obtained through the Barrett–Joyner–Halenda method. Scale bars represent 50 nm in (a,e), 200 nm in (b,c) and 100 nm in (d,e).
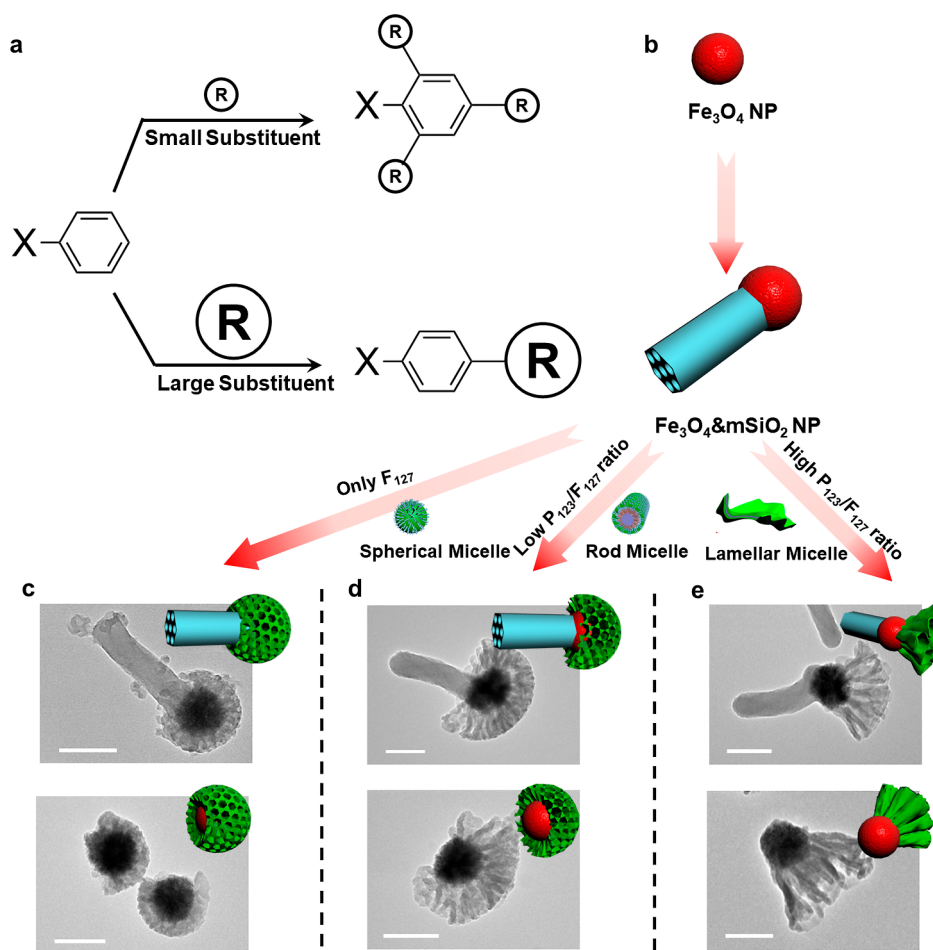
Figure 3. Steric-induced anisotropic assembly of lamellar mesoporous polydopamine. (a) Schematic illustration of a steric effect-induced site selective substitution reaction in organic synthesis. (b−e) Schematic illustration of the morphology evolution and TEM images of the $mSiO_2\&Fe_3O_4\&mPDA$ and $Fe_3O_4\&mPDA$ nanoparticles obtained from different pluronic P_{123}/F_{127} ratio: (c) 0:1, (d) 0.05:0.95, and (e) 0.1:0.9. Scale bars represent 100 nm in all images.

assembly of lamellar mesoporous polydopamine (mPDA) on magnetite Fe_3O_4 nanoparticles, $Fe_3O_4\&mPDA$ Janus nanoparticles with a badminton-like morphology and asymmetric mass distribution are designed and synthesized (Figure 1a). The obtained nanobadmintons possess dual subunits of a high density Fe_3O_4 "head" with a diameter of ~100 nm and a low density mPDA polymeric cone that has a round base with ~250 nm in diameter and ~200 nm in height. The nanoparticles' unique morphology and asymmetric mass distribution significantly affect their fluid dynamics. Computational simulations show that they have a stable fluid posture of mPDA cone facing forward, and the force analyses demonstrate that the unique badminton architecture endows the nanoparticles with a balanced motion around this posture, thus providing a straighter flow trail compared to the spherical $Fe_3O_4@mPDA$ nanoparticles. Owing to the straight moving trails in the bloodstream, the interaction frequency between the nanobadmintons and vascular walls is reduced by about ~50%, which further results in the prolonged blood circulation time, ~40 and ~15% reduction in the cellular uptake and liver uptake over 24 h, respectively (Figure 1b). This work proposed the fabrication of novel badminton-like nanoparticles with an asymmetric mass distribution and systematically probed the linkage among nanoparticles' architecture, biofluid dynamics, organ clearance, and blood circulation, presenting a novel perspective on understanding nanoparticles' in vivo behavior, paving a new way of manufacturing nanomaterials for biomedical fields.

■ RESULTS AND DISCUSSION

As shown in Figure 1, superparamagnetic Fe_3O_4 nanoparticles with a uniform diameter of ~100 nm are first prepared via a solvothermal method (Figure S1).[43] The Janus $mSiO_2\&Fe_3O_4$ ($mSiO_2$ = mesoporous silica) nanoparticles are then fabricated through an anisotropic assembly approach reported previously (Figure S2).[44] By using amphiphilic triblock copolymer pluronic F_{127} and P_{123} as cosurfactants, broom-like triblock $mSiO_2\&Fe_3O_4\&mPDA$ nanoparticles can be obtained based on the steric-induced anisotropic assembly (Figure S3). Further etching of the silica domain results in the $Fe_3O_4\&mPDA$ nanoparticles with badminton-like architectures (Figure 2).

Scanning electron microscopy (SEM) and transmission electron microscopy (TEM) images (Figure S3) of the $mSiO_2\&Fe_3O_4\&mPDA$ nanoparticles demonstrate that the triblock nanoparticles possess a $mSiO_2$ nanorod with a length of ~400 nm and a Fe_3O_4 nanosphere with a diameter of ~100 nm in the middle. The cone-shaped mPDA subunit with the subface facing in the opposite direction of the $mSiO_2$ nanorods is grown selectively on the magnetite Fe_3O_4 domain, and the
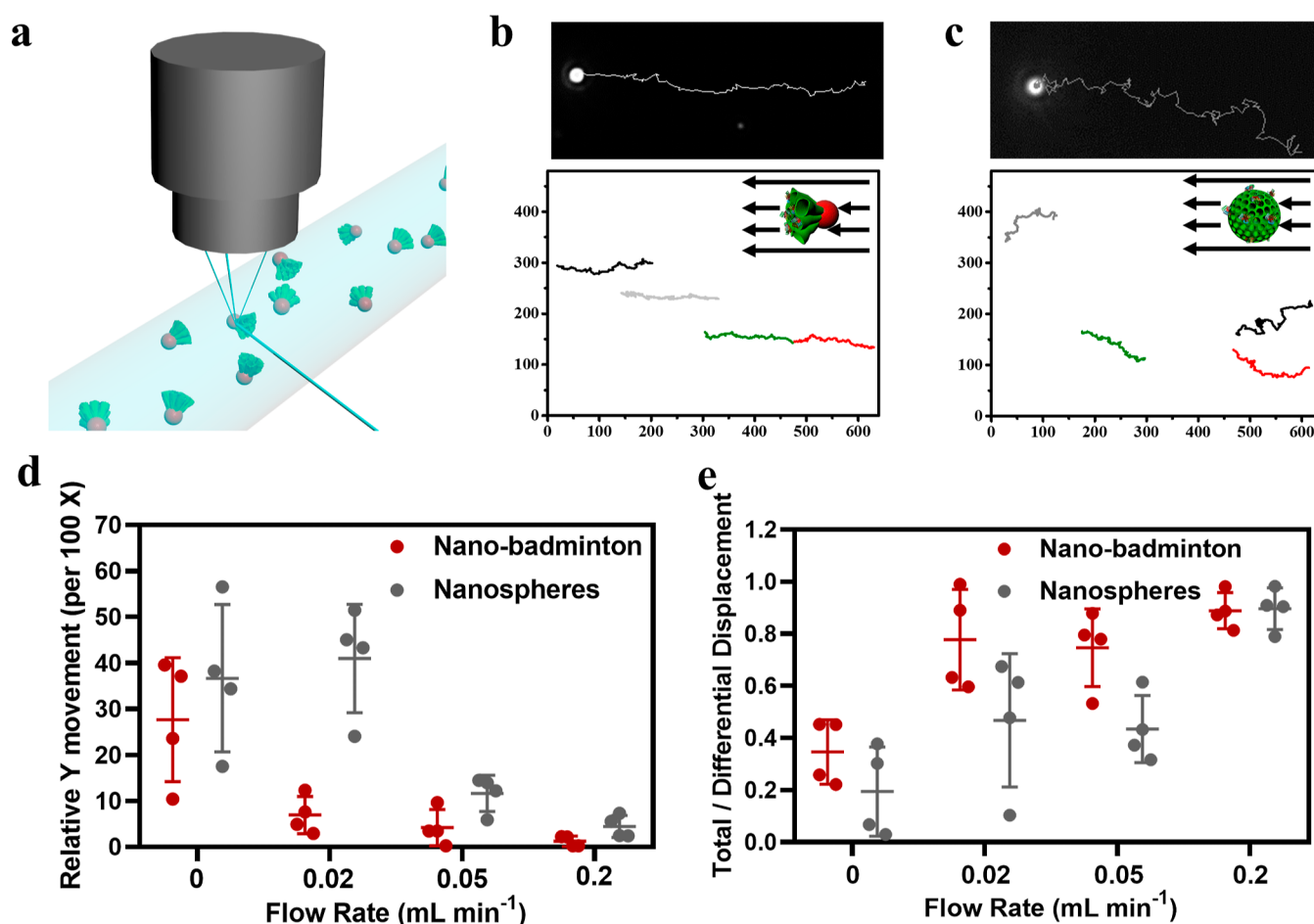
Figure 4. Microfluid-microscope system analysis of particle fluid dynamic. (a) 3D illustration of the microfluid-microscope system of tracking nanoparticles' movements. The dark-field image and particle trail analysis of (b) badminton-like nanoparticles and (c) spherical core@shell nanoparticles under a flow rate of 0.02 mL min⁻¹. (d) Relative Y movement per 100× and (e) ratio between total and differential displacements of the two nanoparticles under various flow rates. X is the horizontal direction of the field of view, and also the direction of flow. Y is the vertical direction of the field of view. Differential displacement is the total length of the move route, and total displacement is the direct distance between the initial and end positions. Scale bars in (b,c) are presented in micrometers. The bars represent mean ± s.d. derived from $n = 4$ groups.

height and diameter of the cones are measured to be about 200 and 250 nm, respectively. The Fe_3O_4&mPDA nanobadmintons, in which the Fe_3O_4 nanoparticles as a "cork" and mPDA cones as a "plume", can be obtained after the hydrothermal etching of $mSiO_2$ nanorods at 100 °C (Figure 2a−d). The morphology and size of the mPDA-truncated cones are retained after hydrothermal treatment. The mPDA domain covers about 1/3 of the surface of the Fe_3O_4 nanoparticles, and mesopores with a diameter of ∼20 nm formed through stacking of lamellar PDA sheets can be observed in each particle (Figure S4). Elemental mappings of the nanoparticles clearly display the asymmetric distribution of Si, Fe, and C elements, demonstrating the anisotropic architectures (Figure S5). In situ tilting observations also demonstrate the asymmetric badminton-like architecture of the Fe_3O_4&mPDA nanoparticles (Figures 2f and S6). The Brunauer−Emmett−Teller surface area of the mesoporous Fe_3O_4&mPDA nanobadmintons is measured to be about 122 m² g⁻¹, which can be attributed to the lamellar wrinkled mesopores composed of PDA (Figure 2g). The average mesopore size is measured to be ∼20 nm, in accordance with SEM and TEM observations. The thermal gravimetric analysis shows that ∼89% of the total weight of the Fe_3O_4&mPDA nanoparticles is contributed by the Fe_3O_4 nanospheres (Figure S7). Modeling calculations

show that the centers of mass of badminton-like Fe_3O_4&mPDA nanoparticles almost coincide with the circular centers of the Fe_3O_4 nanosphere, deviating from the geometric centers of the overall particles. It should be noted that this deviation is not only due to the unique morphology but also relies on the density difference between Fe_3O_4 and PDA. Switching to other asymmetric nanoparticles, such as Fe_3O_4&$mSiO_2$, the center of mass is not far from the geometrical center due to the insufficiently large density difference between the two components, although the overall asymmetry is asymmetric (Figure S8). Overall, we may conclude that this nanoparticle not only morphologically simulating badminton but also imitating badmintons in its asymmetric mass distribution.

To achieve a nanobadminton architecture, the mPDA compartments have to be anisotropically assembled on the magnetite Fe_3O_4 surface. Therefore, a "directing force" is required to orient the assembly direction of the lamellar mPDA. Herein, we take inspiration from the steric effects in organic chemistry and designed a steric-induced anisotropic assembly strategy.

In organic synthesis, the substitution position and orientation of functional groups are significantly influenced by the steric effects (Figure 3a). In a similar fashion, the Janus
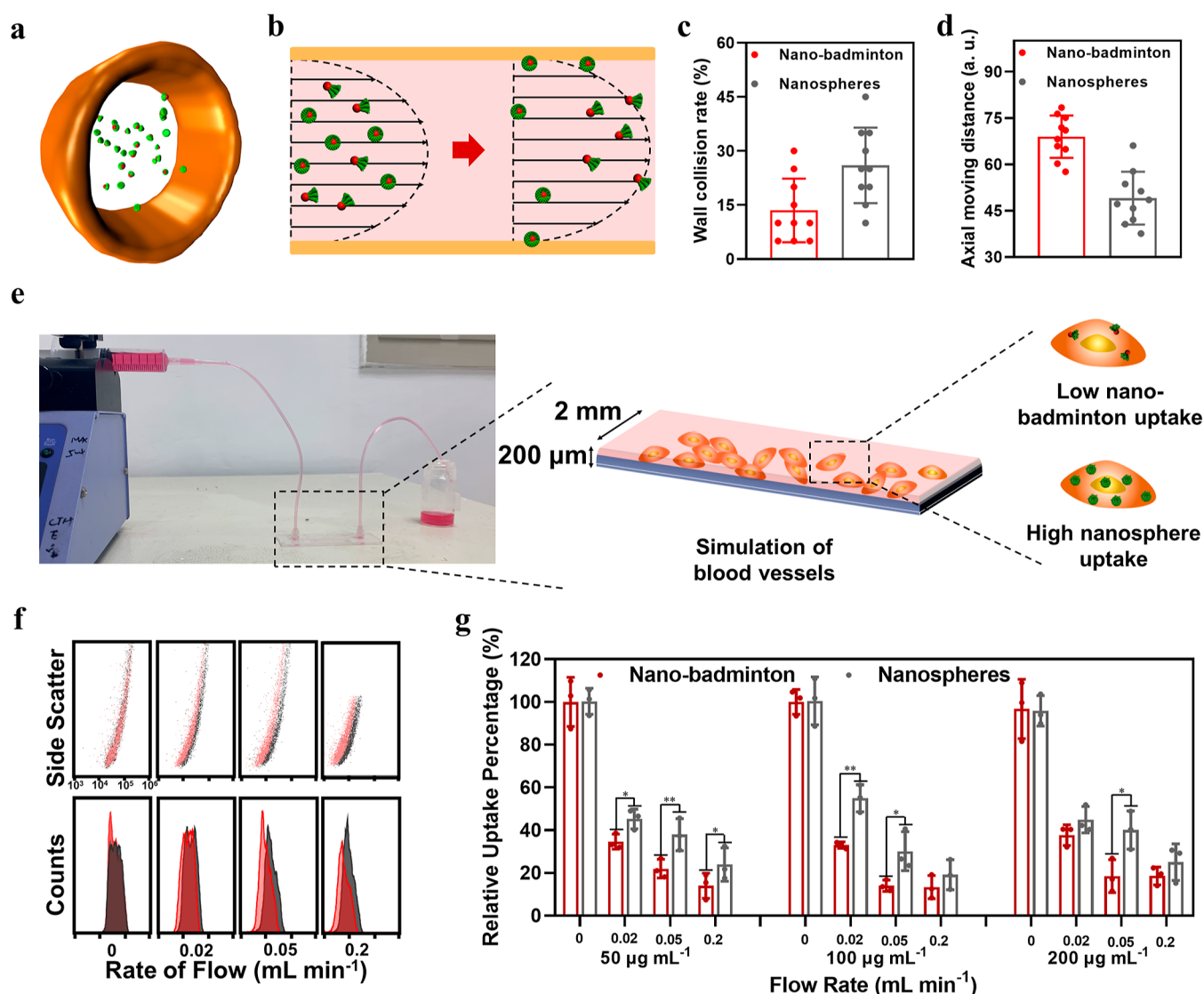
Figure 5. Computation and in vitro simulation of nanoparticles' fluid dynamics in blood vessels. (a) Schematic illustration of simulating nanoparticles' biofluid dynamics in blood vessels using SDPD (b) and how the nanobadmintons tend to move faster and collide less with the vessel wall compared to the nanospheres. (c) Statistics of the rate of encountering with pipeline walls and (d) average moving distance of the two nanoparticles along the pipeline. (e) Schematic illustration of the microfluidic-based artificial "blood vessel". (f) Flow cytometric analysis (100 μg mL^{-1}) and (g) ICP analysis of relative cellular uptake of nanoparticles with varied concentrations and flow speeds. Color red for the nanobadmintons and black for the nanospheres in all data. The bars represent mean ± s.d. derived from (c,d) $n = 10$ and (g) $n = 3$ groups. The statistical analysis was performed by using one-way analysis of variance (ANOVA), followed by the post hoc Tukey's method. *0.01 < P < 0.05, **P < 0.01.

Fe_3O_4&$mSiO_2$ nanoparticles are first fabricated, in which the mesoporous $mSiO_2$ nanorod function as the space-occupying matter to "block" the space around the Fe_3O_4 nanospheres. Then, P_{123}/F_{127}, TMB, and dopamine together form micelles to assembly on the Fe_3O_4 nanoparticle side.[44−46] Due to the steric repelling between mPDA micelles and $mSiO_2$ nanorods, the mPDA micelles are directed to assemble asymmetrically away from the $mSiO_2$ nanorods (Figure 3b−e).

The steric-induced anisotropic assembly process is verified by TEM images of the products obtained with different pluronic P_{123}/F_{127} ratios. It is found that the P_{123}/F_{127} ratio can enormously affect the anisotropic assembly of the mesoporous mPDA (Figures 3b−e and S9). With the increase of the P_{123}/F_{127} ratio, the morphology of the mesopores in mPDA is altered from spherical (0:1) to rod shape (0.05:0.95) and finally lamellar-stacking pores (0.1:0.9, Figure S10), indicating

that the structure of the PDA-surfactant composite micelles is changed from spherical to lamellar. At the same time, the assembly of the mesoporous mPDA on the Fe_3O_4 nanospheres is turned from a homogeneous shell (Figure 3c,d) into an anisotropic cone facing opposite directions of the $mSiO_2$ nanorods (Figure 3d). Further increasing P_{123}/F_{127} ratio results in phase-separated homogeneous growth of large PDA nanosheets rather than heterogeneous growth on the $mSiO_2$&Fe_3O_4 nanoparticles (0.15:0.85, Figure S11). Furthermore, at a high P_{123}/F_{127} ratio, lamellar mPDA micelles can assemble on the bare Fe_3O_4 nanoparticles (without $mSiO_2$ nanorods) to form the core@shell-structured Fe_3O_4@mPDA nanoparticles, yet only with a homogeneously coated mPDA shell (Figure S12).

Based on the above results and theoretical analysis, we propose a steric-induced anisotropic assembly strategy to

explain the formation process of the nanobadminton architectures (Figure S13). During the mPDA assembly, as reported by previous literature studies, with only pluronic F_{127}, small-sized spherical micelles (<10 nm) are formed.[47] The rod-shaped micelles can be generated at a low P_{123}/F_{127} ratio (∼50 nm in length), and a high P_{123}/F_{127} ratio leads to large lamellar micelles (>100 nm).[48] Steric hindrance of the $mSiO_2$ nanorod does not affect the assembly of small-sized spherical micelles, therefore, with only F_{127}, small-sized spherical micelles (<10 nm) uniformly cover all the Fe_3O_4 nanoparticles. The bigger rod-shaped micelles are sterically repelled by the $mSiO_2$ nanorods, so there is a gap between them. The large size of the lamellar micelles leads to strong steric-repelling between the micelles and $mSiO_2$ nanorods, thus directing the mPDA to assemble anisotropically away from the $mSiO_2$ nanorods, forming the mesoporous mPDA cone. Further increasing pluronic P_{123} ration leads to even larger lamellar micelles, which thus are totally repelled from the $mSiO_2\&Fe_3O_4$ nanoparticles. Also, without the $mSiO_2$ nanorods as the space-occupying matter, the lamellar mPDA micelles would also be unable to achieve anisotropic assembly (Figure S12).

To verify the effect of the architecture on nanoparticles' fluid dynamics, the conventional spherical core@shell-structured Fe_3O_4@mPDA nanoparticles were prepared (Figure S14) and used as the control group in comparison to the badminton-shaped $Fe_3O_4\&$mPDA nanoparticles. The two kinds of particles are made of Fe_3O_4 and mPDA with no variations in compositions. After modification with bovine serum proteins (BSA), the two nanoparticles have nearly identical dynamic light scattering size and surface charge (Figure S15), enabling us to investigate the effect of the architecture on nanoparticles' fluid dynamics with the minimum interferences.

Herein, a dark-field optical microscope combined with a microfluid system is used to record the trajectories of the nanoparticles in the microfluids (Figure 4a). The Brownian movements of two kinds of nanoparticles are similar under static conditions (Figure S16). However, in microfluids with a flow rate of 0.02 mL min^{-1}, the badminton-like nanoparticles have more obvious linear trails (Figure 4b) compared to the spherical-shaped core@shell nanoparticles, where the trails are zigzag ones (Figure 4c). The difference in the trajectory patterns induced by the variety in architectures can also be observed at a high flow rate (Figure S17). The analysis of the trajectories demonstrates that the spherical nanoparticles have larger movements in the cross-flow direction (Figure 4d), which is three times higher than the nanobadmintons. The ratio between the nanoparticles' linear displacement (the distance between the start and end location) and travel distance (adding up the distance of each step) is calculated (Figure 4e), which can be used to evaluate the linearity of the trails. The closer to 1 this value is, the more linear the movement. While the value for the nanospheres is below 0.5 in different flow rates, the value for the nanobadmintons is near 1 (>0.8) under all fluid speeds, indicating a good linearity of the moving trails. The spherical nanoparticles have ∼50% lower downstream speed at 0.02 mL min^{-1} and ∼15% less at 0.2 mL min^{-1} (Figure S18). The plane diffusion coefficient of the two kinds of nanoparticles also evidence that the badminton-like nanoparticles possess a higher speed in flowing fluid, a ∼30% differential at a high flow rate (Figure S19). Overall, these results clearly demonstrate that the badminton-like architecture may endow nanoparticles with more stable dynamics and linear trails in flowing fluid.

Computation modeling based on the smooth dissipative particle dynamics (SDPD) method is used for systematic simulation of the nanoparticles' movements and encounter with pipe walls in a flowing fluid (Figure 5a). The results demonstrate that the nanobadmintons move much faster in the fluid and encounter less with pipe walls (Figure 5b). On a simulation run of 10 times, with 20 nanoparticles starting, an average of ∼14% of the nanobadmintons can interact with the pipeline (Figure 5c), which is almost half the amount compared to the core@shell-structured nanospheres (∼27%). "Snapshots" are taken at randomly selected moments, and it can be clearly observed that the majority of the nano-badmintons have their "cone" facing forward (Figure S20). The simulation also demonstrates that the nanobadmintons undertake smaller radius forces (Figure S21) and have a lower mean square value of moving distance in the pipeline radius direction compared to the core@shell-structured nanospheres (Figure S22). These results are much in agreement with previous dark-field observations that the nanobadmintons have straighter trails and less probability of encountering pipeline margin. Finally, simulation results show that over the same period, the nanobadmintons have a longer down-flow moving distance (∼40%, Figure 5d), indicating that they have a faster down-flow moving distance than the core@shell nanospheres. Such simulations clearly verify that the nanobadmintons have better linear trails and less probability of encountering pipeline margins. Altogether, the computational simulation demonstrates that the nanobadminton architecture provides nanoparticles with more stable fluid dynamics and less chance of margination.

Based on the above observations that the badminton-like architecture endows nanoparticles with less probability of encountering pipeline walls, we further investigated how such fluid dynamics could affect the nanobio interaction by using a homemade vascular simulation setup. An injection pump and a HUVEC endothelial cells adherent grown single channel chip (2 mm × 200 μm) were utilized for in vitro simulations of the nanoparticles' vascular flowing (Figure 5e).[32,34] The pump provided flowing of "blood", and the cell-grown chips function as an artificial "blood vessel". The two kinds of the nanoparticles (nanobadmintons and nanospheres) were modified with indocyanine green@bovine serum albumin (ICG@BSA) or DOX@BSA (DOX = doxorubicin) complexes, which allowed both in vitro and in vivo monitoring of the nanoparticles (Figures S23 and S24).[49−51] The synthesized nanoparticles demonstrated superior biocompatibility in vitro and in vivo experiments. No significant cytotoxicity was observed at high concentrations (600 μg/mL, Figure S25). Acute toxicology experiments also confirmed that injection at a high concentration (1 mg/kg) did not cause stressful death in mice. The cellular uptake of nanoparticles was investigated by confocal laser scanning microscopy (CLSM), flow cytometric analysis, and inductively coupled plasma (ICP). No significant differences between the two nanoparticles can be observed under static conditions. At the same time, we examined the phagocytic pathway of cellular uptake of both by inhibitor experiments. The experimental results demonstrate that both are taken up via energy-dependent and clathrin-mediated pathways, and the effects of inhibitors on the cellular uptake of both are consistent, proving that the morphological changes do not affect the pathway of the cellular uptake of nanoparticles (Figure S26). For both nanoparticles, the cellular internalization is reduced upon the flowing of the nanoparticles'

Journal of the American Chemical Society
pubs.acs.org/JACS
Article
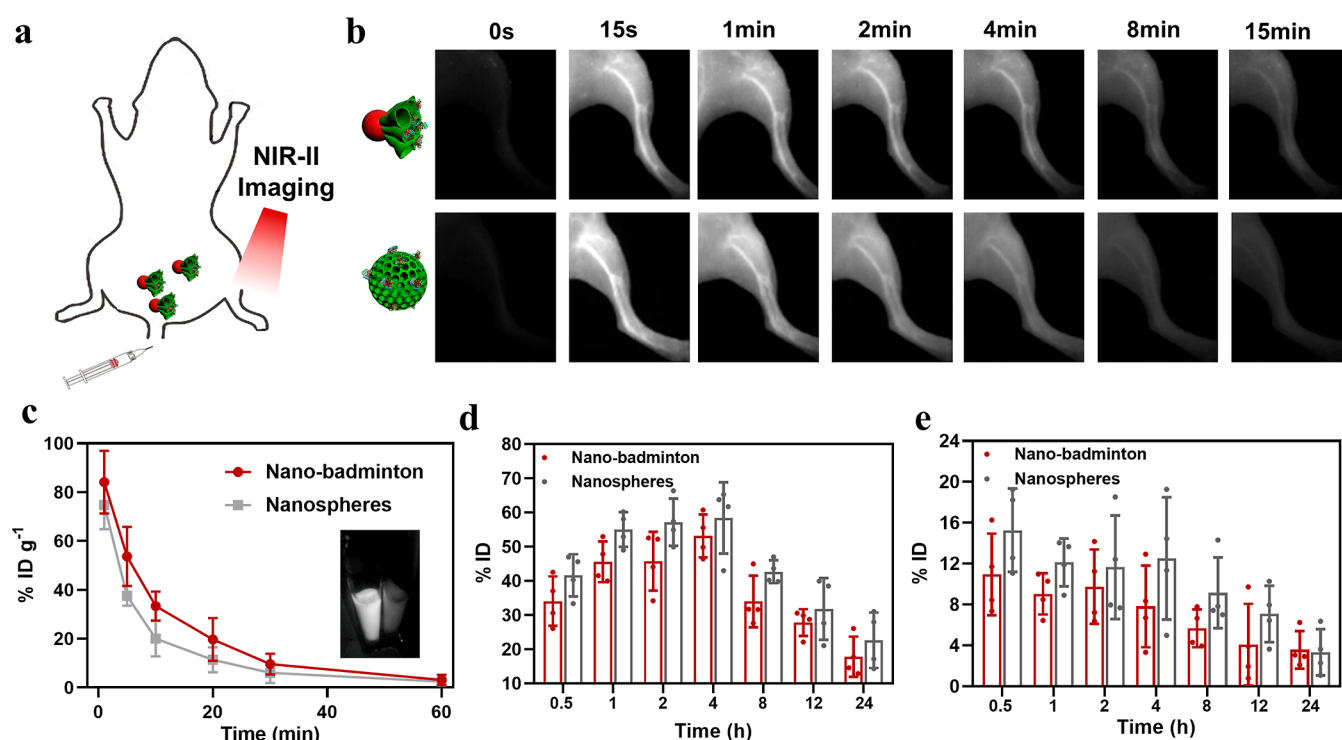
Figure 6. In vivo blood circulation and organ uptake of the nanoparticles. (a) Schematic illustration of the analysis of nanoparticles' blood circulation time by using NIR-II imaging. The two nanoparticles are loaded with indocyanine green, and their concentrations in the mouse hindlimb vessels are imaged under a radiation of 808 nm light using CCD. (b) NIR-II imaging of the mice hindlimb vessels. Nanoparticles were quickly injected through tail vein and then the NIR-II intensity was monitored. For the nanobadmintons, the hindlimb vessel is still clearly observable at 15 min, while that of nanospheres is difficult to distinguish, demonstrating that badminton-like nanoparticles have longer blood circulation comparing to nanospheres. (c) Concentrations of the nanoparticles in the blood within 1.0 h after injection. The accumulation of the nanoparticles in the (d) liver and (e) lung at various time points postinjection. Nanoparticles are quickly injected through the tail vein; at various time points, blood is collected from orbit, and organs are acquired from sacrificed mice. Intensity of indocyanine green is used to reveal the concentration of the two nanoparticles within the blood and organs. The bars represent mean ± s.d. derived from $n = 4$ groups.

medium solution regardless of architectures. Yet, the uptake rate of the nanobadmintons is less than that of the nanospheres under all three flowing speeds (Figure S27). Taking the cellular uptake under the static condition as an example, the internalization of the nanobadmintons has as much as ∼15% reduction compared to that of the nanospheres (22% vs 38%, 0.02 mL min^{-1} flow rate, Figures 5f,g and S28). The cellular uptake of the nanobadmintons is lower than that of the nanospheres under all particle concentrations and flowing speed, clearly demonstrating that the badminton architecture can reduce the nanobio interaction based on the unique fluid dynamics.

The above results demonstrate that the badminton-like architecture may provide the nanoparticles with more stable fluid dynamics, linear motions, reduced interaction frequency with blood vessel walls, and lower cellular uptake under flowing fluid. We assume that because the nanoparticles with a diameter ranging in 100−500 nm are mainly cleared via the phagocytosis by endothelium and Kupffer cells on the liver sinusoid vascular walls[31] such reduced interaction frequency should lower nanoparticles' liver uptake efficiency and prolong blood circulation time. After functioning with the ICG@BSA complexes, the fluorescence of the nanoparticles in the NIR-II region can be stable for a long period, allowing analysis of the concentration effects (Figures S23 and S29). NIR-II imaging of mice hindlimb vessels demonstrates that while the vessels are illumined simultaneously upon injection for the two kinds of nanoparticles, the fluorescence intensity of mice injected with

the badminton-like nanoparticles decayed much slower than that of the spherical nanoparticles (Figure 6a). The difference in intensity is already significant at 4 min. At 15 min, the vessel of mice injected with the badminton-like nanoparticles is still visible, while the intensity with the spherical core@shell nanoparticles has completely vanished (Figure 6b). The nanoparticle concentration in blood was further investigated by phlebotomizing at different time points postinjection and quantified based on fluorescence intensity. A blood circulation half-life time of 0.15 h is observed for the badminton-like nanoparticles, which is a doubled period compared to 0.069 h for the spherical core@shell-structured nanoparticles (Figure 6c). Such differences in fluorescence decaying and blood circulation half-life time indicate that the spherical nanoparticles have faster a bloodstream than the badminton-like nanoparticles, which can be attributed to the architecture-induced varied biofluid dynamics. The mice were sacrificed at different times postinjection, and the liver and lungs were collected to investigate the biodistribution of the injected nanoparticles. The ICP measurements of the liver (Figure 6d) and lungs (Figure 6e), the two organs mainly responsible for the clearance of nanoparticles, clearly reveal that the badminton-like nanoparticles have an ∼15% lower uptake efficiency in the liver and ∼25% reduction in the lung, compared to the spherical ones. The distribution of the nanoparticles in other organs also indicates similar results (Figure S30). The blood circulation time and organ uptake assessments together verify the above-mentioned hypothesis:
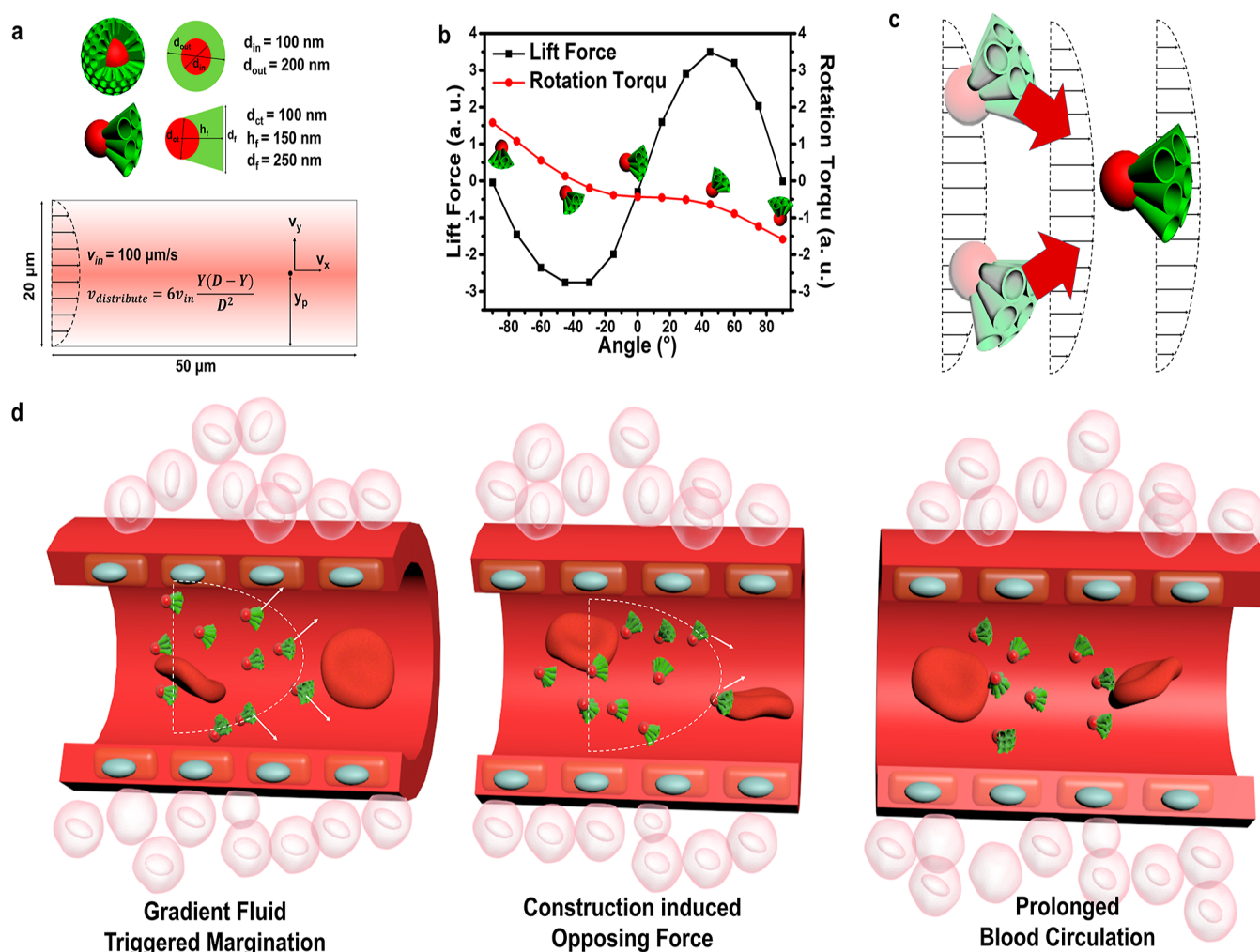
Figure 7. Mechanism of the nanobadmintons' unique blood flow dynamics. (a) Models of the badminton-like Fe_3O_4&mPDA nanoparticle, spherical core@shell-structured Fe_3O_4@mPDA nanoparticle, and the pipeline with graded distributed fluid flow in the finite element analysis. (b) Diagram of the rotation torque and lift force that the nanobadmintons undertake with different tilting angles in the upper part of the pipeline. (c) Schematic illustration of the nanobadmintons' "balanced motion" in fluid. Red arrows are representations of the force undertaken from fluid. The nanobadmintons always undertake forces pointing toward the center. (d) Schematic illustration of the mechanism of the nanobadmintons' unique bloodstream dynamics.

the relatively stable biofluid dynamics may reduce interaction frequency between the badminton-shaped nanoparticles and vascular vessels, further decreasing uptake efficiency by endothelium cells, lowering organ clearance rate, and prolonging blood circulation time.

Based on the Fe_3O_4&mPDA nanoparticle's unique badminton-like morphology and asymmetric mass distribution, computation simulation was conducted to investigate the relationship between nanoparticles' architecture, fluid dynamics, and blood vessel margination. Theoretical models were established based on the finite element analysis method and used for nanoparticles' force analysis; the down-flow direction is set as x and that vertical to the pipe is set as y (Figure 7a). As demonstrated by the nephogram of flow speed distributions, the torque is zero when the nanobadminton takes a position with the "cone" facing forward; thus, this is the most stable posture of the nanobadmintons in flowing fluid (Figures 7b, S31 and S32). When a dip angle exists between the nanobadminton's axis and the fluid direction (x), the torque is not zero and pointing toward the axis of symmetry,

indicating that the nanobadmintons will rotate to be aligned with the fluid direction (Figure S33).

The influence of the nanoparticle's mass distribution on impact and motion is also simulated. Due to the asymmetric mass distribution of the nanobadmintons, the majority of mass is concentrated in the Fe_3O_4 nanoparticle "head", while the mPDA "plume" has a low density but with a larger area for force application. Consequently, during impact, the "head" and "plume" experience different accelerations, leading to the nanobadminton's rotational motion (Figures 7b and S34). With rotation, the fluid's impact on the nanobadminton could eventually change and varies with different contact angles. This phenomenon is distinct from that in symmetric nanoparticles, where the center of mass coincides with the geometric center.

Based on the above simulation results, we propose a "balanced motion" to explain the linear movement of the nanobadmintons, which is attributed to the unique badminton-like morphology and mass distribution of the nanobadmintons (Figure 7c,d). When the nanobadmintons undertake forces in the vertical directions, the asymmetric mass distribution provide a strong tendency for the nanobadmintons to rotate.

Now the nanobadmintons have an angle that deviates the most stable posture, a torque is generated, which pushes them back to their original position. The nanobadmintons are pushed back both in the posture and position. This process keeps on repeating itself; the nanobadmintons are hence in a dynamics balance in the flowing fluid and do not have as much tendency to move vertically as nanospheres (Figure 7c). The nanospheres, on the other hand, undertake a constant vertical y-direction force pointing toward the pipeline wall, which is due to the gradient distribution of fluid velocity in the pipeline (Figure S35). Therefore, nanospheres always have a strong tendency of margination toward vessel walls, being captured by cells on the vessel walls, eliminated from the blood circulation, and accumulated in organs.[25] This hypothesis may well explain how the badminton-like morphology and mass distribution may provide nanoparticles with more stable flow dynamics.

CONCLUSIONS

Inspired by the unique aerodynamics of badmintons, the magnetite nano-Fe_3O_4&mPDA nanobadmintons with an asymmetric mass distribution have successfully been synthesized through a novel steric-induced anisotropic assembly strategy. The nanobadmintons' architecture significantly affects their fluid dynamics, providing a straighter flow trail compared to the spherical Fe_3O_4@mPDA nanoparticles. Computational simulations show that the nanobadmintons have a stable fluid posture of the mPDA cone facing forward, and force analysis demonstrates that the unique badminton-like morphology and mass distribution endows the nanoparticles with a balanced motion around this posture, making its movement in fluid stable. The straight moving trails enable nanobadmintons ~50% reduced interaction frequencies with blood vascular walls, and therefore, ~40% reduced cellular uptake, ~15% less liver uptake, and doubled blood circulation half-life in the same time period. This research presents a novel approach to fabricating badminton-like nanoparticles with an asymmetric mass distribution. It systematically explores the interconnections between the nanoparticles' architecture, biofluid dynamics, organ clearance, and blood circulation, offering a unique perspective on comprehending the in vivo behavior of nanoparticles. Moreover, this work lays the groundwork for the advancement of nanomaterial manufacturing in biomedical applications.

ASSOCIATED CONTENT

Ⓢ Supporting Information

The Supporting Information is available free of charge at https://pubs.acs.org/doi/10.1021/jacs.3c07097.

> Experimental details, materials, methods, TEM, SEM, dark-field TEM, thermal gravimetric analysis, schematic illustration, dynamic light scattering, particle trail analysis, diffusion coefficient, mean square value, NIR-II imaging, UV-vis, nephogram, simulation result, and CLSM (PDF)

AUTHOR INFORMATION

Corresponding Authors

Xiaomin Li − *Department of Chemistry, Laboratory of Advanced Materials and Shanghai Key Laboratory of Molecular Catalysis and Innovative Materials, State Key Laboratory of Molecular Engineering of Polymers, Collaborative Innovation Center of Chemistry for Energy Materials (2011-iChEM), School of Chemistry and Materials, Fudan University, Shanghai 200433, P. R. China;* ◉ orcid.org/0000-0001-6056-6928; Email: lixm@fudan.edu.cn

Dongyuan Zhao − *Department of Chemistry, Laboratory of Advanced Materials and Shanghai Key Laboratory of Molecular Catalysis and Innovative Materials, State Key Laboratory of Molecular Engineering of Polymers, Collaborative Innovation Center of Chemistry for Energy Materials (2011-iChEM), School of Chemistry and Materials, Fudan University, Shanghai 200433, P. R. China;* ◉ orcid.org/0000-0001-8440-6902; Email: dyzhao@fudan.edu.cn

Authors

Tiancong Zhao − *Department of Chemistry, Laboratory of Advanced Materials and Shanghai Key Laboratory of Molecular Catalysis and Innovative Materials, State Key Laboratory of Molecular Engineering of Polymers, Collaborative Innovation Center of Chemistry for Energy Materials (2011-iChEM), School of Chemistry and Materials, Fudan University, Shanghai 200433, P. R. China*

Runfeng Lin − *Department of Chemistry, Laboratory of Advanced Materials and Shanghai Key Laboratory of Molecular Catalysis and Innovative Materials, State Key Laboratory of Molecular Engineering of Polymers, Collaborative Innovation Center of Chemistry for Energy Materials (2011-iChEM), School of Chemistry and Materials, Fudan University, Shanghai 200433, P. R. China*

Borui Xu − *Department of Materials Science, State Key Laboratory of ASIC and Systems, Fudan University, Shanghai 200433, P. R. China;* ◉ orcid.org/0000-0001-5357-0400

Minchao Liu − *Department of Chemistry, Laboratory of Advanced Materials and Shanghai Key Laboratory of Molecular Catalysis and Innovative Materials, State Key Laboratory of Molecular Engineering of Polymers, Collaborative Innovation Center of Chemistry for Energy Materials (2011-iChEM), School of Chemistry and Materials, Fudan University, Shanghai 200433, P. R. China*

Liang Chen − *Department of Chemistry, Laboratory of Advanced Materials and Shanghai Key Laboratory of Molecular Catalysis and Innovative Materials, State Key Laboratory of Molecular Engineering of Polymers, Collaborative Innovation Center of Chemistry for Energy Materials (2011-iChEM), School of Chemistry and Materials, Fudan University, Shanghai 200433, P. R. China*

Fan Zhang − *Department of Chemistry, Laboratory of Advanced Materials and Shanghai Key Laboratory of Molecular Catalysis and Innovative Materials, State Key Laboratory of Molecular Engineering of Polymers, Collaborative Innovation Center of Chemistry for Energy Materials (2011-iChEM), School of Chemistry and Materials, Fudan University, Shanghai 200433, P. R. China;* ◉ orcid.org/0000-0001-7886-6144

Yongfeng Mei − *Department of Materials Science, State Key Laboratory of ASIC and Systems, Fudan University, Shanghai 200433, P. R. China;* ◉ orcid.org/0000-0002-3314-6108

Complete contact information is available at:
https://pubs.acs.org/10.1021/jacs.3c07097

Notes

The authors declare no competing financial interest.

■ REFERENCES

(1) Choi, H.; Liu, W.; Liu, F.; Nasr, K.; Misra, P.; Bawendi, M. G.; Frangioni, J. V. Design considerations for tumour-targeted nanoparticles. *Nat. Nanotechnol.* 2010, 5, 42−47.

(2) Kevadiya, B.; Ottemann, B. M.; Thomas, M. B.; Mukadam, I.; Nigam, S.; McMillan, J.; Gorantla, S.; Bronich, T. K.; Edagwa, B.; Gendelman, H. E. Neurotheranostics as personalized medicines. *Adv. Drug Delivery Rev.* 2019, 148, 252−289.

(3) Sang, W.; Zhang, Z.; Dai, Y.; Chen, X. Recent advances in nanomaterial-based synergistic combination cancer immunotherapy. *Chem. Soc. Rev.* 2019, 48, 3771−3810.

(4) Janjua, T.; Cao, Y.; Yu, C.; Popat, A. Clinical translation of silica nanoparticles. *Nat. Rev. Mater.* 2021, 6, 1072−1074.

(5) Jiang, W.; Wang, Y.; Wargo, J.; Lang, F.; Kim, B. Considerations for designing preclinical cancer immune nanomedicine studies. *Nat. Nanotechnol.* 2021, 16, 6−15.

(6) Gong, N.; Sheppard, N.; Billingsley, M.; June, C.; Mitchell, M. Nanomaterials for T-cell cancer immunotherapy. *Nat. Nanotechnol.* 2021, 16, 25−36.

(7) de Lazaro, I.; Mooney, D. Obstacles and opportunities in a forward vision for cancer nanomedicine. *Nat. Mater.* 2021, 20, 1469−1479.

(8) Wang, Y.; Cai, R.; Chen, C. The nano-bio interactions of nanomedicines: understanding the biochemical driving forces and redox reactions. *Acc. Chem. Res.* 2019, 52, 1507−1518.

(9) Blanco, E.; Shen, H.; Ferrari, M. Principles of nanoparticle design for overcoming biological barriers to drug delivery. *Nat. Biotechnol.* 2015, 33, 941−951.

(10) Poon, W.; Kingston, B.; Ouyang, B.; Ngo, W.; Chan, W. A framework for designing delivery systems. *Nat. Nanotechnol.* 2020, 15, 819−829.

(11) Hong, E.; Dobrovolskaia, M. Addressing barriers to effective cancer immunotherapy with nanotechnology: achievements, challenges, and roadmap to the next generation of nanoimmunotherapeutics. *Adv. Drug Delivery Rev.* 2019, 141, 3−22.

(12) Degors, I.; Wang, C.; Rehman, Z.; Zuhorn, I. Carriers break barriers in drug delivery: endocytosis and endosomal escape of gene delivery vectors. *Acc. Chem. Res.* 2019, 52, 1750−1760.

(13) Lane, L.; Qian, X.; Smith, A.; Nie, S. Physical chemistry of nanomedicine: understanding the complex behaviors of nanoparticles in vivo. *Annu. Rev. Phys. Chem.* 2015, 66, 521−547.

(14) Rennick, J.; Johnston, A.; Parton, R. Key principles and methods for studying the endocytosis of biological and nanoparticle therapeutics. *Nat. Nanotechnol.* 2021, 16, 266−276.

(15) Ouyang, B.; Poon, W.; Zhang, Y. N.; Lin, Z. P.; Kingston, B. R.; Tavares, A. J.; Zhang, Y.; Chen, J.; Valic, M. S.; Syed, A. M.; et al. The dose threshold for nanoparticle tumour delivery. *Nat. Mater.* 2020, 19, 1362−1371.

(16) Chen, F.; Madajewski, B.; Ma, K.; Karassawa Zanoni, D.; Stambuk, H.; Turker, M. Z.; Monette, S.; Zhang, L.; Yoo, B.; Chen, P.; et al. Molecular phenotyping and image-guided surgical treatment of melanoma using spectrally distinct ultrasmall core-shell silica nanoparticles. *Sci. Adv.* 2019, 5, No. eaax5208.

(17) Zhao, T.; Wang, P.; Li, Q.; Al-Khalaf, A. A.; Hozzein, W. N.; Zhang, F.; Li, X.; Zhao, D. Near-infrared triggered decomposition of nanocapsules with high tumor accumulation and stimuli responsive fast elimination. *Angew. Chem., Int. Ed.* 2018, 57, 2611−2615.

(18) Chen, L.; Zhao, T.; Zhao, M.; Wang, W.; Sun, C.; Liu, L.; Li, Q.; Zhang, F.; Zhao, D.; Li, X. Size and charge dual-transformable mesoporous nanoassemblies for enhanced drug delivery and tumor penetration. *Chem. Sci.* 2020, 11, 2819−2827.

(19) Kolhar, P.; Anselmo, A. C.; Gupta, V.; Pant, K.; Prabhakarpandian, B.; Ruoslahti, E.; Mitragotri, S. Using shape effects to target antibody-coated nanoparticles to lung and brain endothelium. *Proc. Natl. Acad. Sci. U.S.A.* 2013, 110, 10753−10758.

(20) Zhao, T.; Chen, L.; Wang, P.; Li, B.; Lin, R.; Abdulkareem Al-Khalaf, A.; Hozzein, W. N.; Zhang, F.; Li, X.; Zhao, D. Surface-kinetics mediated mesoporous multipods for enhanced bacterial adhesion and inhibition. *Nat. Commun.* 2019, 10, 4387.

(21) Abbaraju, P.; Meka, A. K.; Song, H.; Yang, Y.; Jambhrunkar, M.; Zhang, J.; Xu, C.; Yu, M.; Yu, C. Asymmetric silica nanoparticles with tunable head-tail structures enhance hemocompatibility and maturation of immune cells. *J. Am. Chem. Soc.* 2017, 139, 6321−6328.

(22) Suk, J.; Xu, Q.; Kim, N.; Hanes, J.; Ensign, L. PEGylation as a strategy for improving nanoparticle-based drug and gene delivery. *Adv. Drug Delivery Rev.* 2016, 99, 28−51.

(23) Liu, Z.; Davis, C.; Cai, W.; He, L.; Chen, X.; Dai, H. Circulation and long-term fate of functionalized, biocompatible single-walled carbon nanotubes in mice probed by Raman spectroscopy. *Proc. Natl. Acad. Sci. U.S.A.* 2008, 105, 1410−1415.

(24) Han, X.; Lu, Y.; Xie, J.; Zhang, E.; Zhu, H.; Du, H.; Wang, K.; Song, B.; Yang, C.; Shi, Y.; et al. Zwitterionic micelles efficiently deliver oral insulin without opening tight junctions. *Nat. Nanotechnol.* 2020, 15, 605−614.

(25) Tang, S.; Peng, C.; Xu, J.; Du, B.; Wang, Q.; Vinluan, R. D.; Yu, M.; Kim, M. J.; Zheng, J. Tailoring renal clearance and tumor targeting of ultrasmall metal nanoparticles with particle density. *Angew. Chem., Int. Ed.* 2016, 55, 16039−16043.

(26) Bjornmalm, M.; Faria, M.; Chen, X.; Cui, J.; Caruso, F. Dynamic flow impacts cell-particle interactions: sedimentation and particle shape effects. *Langmuir* 2016, 32, 10995−11001.

(27) Hu, X.; Sun, J.; Li, F.; Li, R.; Wu, J.; He, J.; Wang, N.; Liu, J.; Wang, S.; Zhou, F.; et al. Renal-clearable hollow bismuth subcarbonate nanotubes for tumor targeted computed tomography imaging and chemoradiotherapy. *Nano Lett.* 2018, 18, 1196−1204.

(28) Kuwahira, I.; Gonzalez, N.; Heisler, N.; Piiper, J. Changes in regional blood flow distribution and oxygen supply during hypoxia in conscious rats. *J. Appl. Physiol.* 1993, 74, 211−214.

(29) Rosenblum, W. Erythrocyte velocity and a velocity pulse in minute blood vessels on the surface of the mouse brain. *Circ. Res.* 1969, 24, 887−892.

(30) Poon, W.; Zhang, Y. N.; Ouyang, B.; Kingston, B. R.; Wu, J. L. Y.; Wilhelm, S.; Chan, W. C. W. Elimination pathways of nanoparticles. *ACS Nano* 2019, 13, 5785−5798.

(31) Tsoi, K.; MacParland, S. A.; Ma, X. Z.; Spetzler, V. N.; Echeverri, J.; Ouyang, B.; Fadel, S. M.; Sykes, E. A.; Goldaracena, N.; Kaths, J. M.; et al. Mechanism of hard-nanomaterial clearance by the liver. *Nat. Mater.* 2016, 15, 1212−1221.

(32) Chen, Y.; Syed, A.; MacMillan, P.; Rocheleau, J.; Chan, W. Flow rate affects nanoparticle uptake into endothelial cells. *Adv. Mater.* 2020, 32, No. e1906274.

(33) Muller, K.; Fedosov, D.; Gompper, G. Margination of micro- and nano-particles in blood flow and its effect on drug delivery. *Sci. Rep.* 2014, 4, 4871.

(34) Vu, M.; Kelly, H. G.; Wheatley, A. K.; Peng, S.; Pilkington, E. H.; Veldhuis, N. A.; Davis, T. P.; Kent, S. J.; Truong, N. P. Cellular

interactions of liposomes and pisa nanoparticles during human blood flow in a microvascular network. *Small* **2020**, *16*, No. e2002861.

(35) Fish, M.; Banka, A. L.; Braunreuther, M.; Fromen, C. A.; Kelley, W. J.; Lee, J.; Adili, R.; Holinstat, M.; Eniola-Adefeso, O. Deformable microparticles for shuttling nanoparticles to the vascular wall. *Sci. Adv.* **2021**, *7*, No. eabe0143.

(36) Zhang, F.; Zhuang, J.; Li, Z.; Gong, H.; de Ávila, B. E. F.; Duan, Y.; Zhang, Q.; Zhou, J.; Yin, L.; Karshalev, E.; et al. Nanoparticle-modified microrobots for in vivo antibiotic delivery to treat acute bacterial pneumonia. *Nat. Mater.* **2022**, *21*, 1324−1332.

(37) Fu, X.; Huck, D.; Makein, L.; Armstrong, B.; Willen, U.; Freeman, T. Effect of particle shape and size on flow properties of lactose powders. *Particuology* **2012**, *10*, 203−208.

(38) Cleary, P. The effect of particle shape on simple shear flows. *Powder Technol.* **2008**, *179*, 144−163.

(39) Zhao, T.; Zhang, X.; Lin, R.; Chen, L.; Sun, C.; Chen, Q.; Hung, C. T.; Zhou, Q.; Lan, K.; Wang, W.; et al. Surface-confined winding assembly of mesoporous nanorods. *J. Am. Chem. Soc.* **2020**, *142*, 20359−20367.

(40) Zhao, T.; Elzatahry, A.; Li, X.; Zhao, D. Single-micelle-directed synthesis of mesoporous materials. *Nat. Rev. Mater.* **2019**, *4*, 775−791.

(41) Fu, J.; Jiao, J.; Ban, W.; Kong, Y.; Gu, Z.; Song, H.; Huang, X.; Yang, Y.; Yu, C. Large scale synthesis of self-assembled shuttlecock-shaped silica nanoparticles with minimized drag as advanced catalytic nanomotors. *Chem. Eng. J.* **2021**, *417*, 127971.

(42) Ma, X.; Hahn, K.; Sanchez, S. Catalytic mesoporous Janus nanomotors for active cargo delivery. *J. Am. Chem. Soc.* **2015**, *137*, 4976−4979.

(43) Liu, J.; Sun, Z.; Deng, Y.; Zou, Y.; Li, C.; Guo, X.; Xiong, L.; Gao, Y.; Li, F.; Zhao, D. Highly water-dispersible biocompatible magnetite particles with low cytotoxicity stabilized by citrate groups. *Angew. Chem., Int. Ed.* **2009**, *48*, 5875−5879.

(44) Zhao, T.; Zhu, X.; Hung, C. T.; Wang, P.; Elzatahry, A.; Al-Khalaf, A. A.; Hozzein, W. N.; Zhang, F.; Li, X.; Zhao, D. Spatial isolation of carbon and silica in a single janus mesoporous nanoparticle with tunable amphiphilicity. *J. Am. Chem. Soc.* **2018**, *140*, 10009−10015.

(45) Peng, L.; Peng, H.; Liu, Y.; Wang, X.; Hung, C. T.; Zhao, Z.; Chen, G.; Li, W.; Mai, L.; Zhao, D. Spiral self-assembly of lamellar micelles into multi-shelled hollow nanospheres with unique chiral architecture. *Sci. Adv.* **2021**, *7*, No. eabi7403.

(46) Peng, L.; Peng, H.; Li, W.; Zhao, D. Monomicellar assembly to synthesize structured and functional mesoporous carbonaceous nanomaterials. *Nat. Protoc.* **2023**, *18*, 1155−1178.

(47) Peng, L.; Hung, C. T.; Wang, S.; Zhang, X.; Zhu, X.; Zhao, Z.; Wang, C.; Tang, Y.; Li, W.; Zhao, D. Versatile nanoemulsion assembly approach to synthesize functional mesoporous carbon nanospheres with tunable pore sizes and architectures. *J. Am. Chem. Soc.* **2019**, *141*, 7073−7080.

(48) Guan, B.; Zhang, S.; Lou, X. Realization of walnut-shaped particles with macro-/mesoporous open channels through pore architecture manipulation and their use in electrocatalytic oxygen reduction. *Angew. Chem., Int. Ed.* **2018**, *57*, 6176−6180.

(49) Carr, J. A.; Franke, D.; Caram, J. R.; Perkinson, C. F.; Saif, M.; Askoxylakis, V.; Datta, M.; Fukumura, D.; Jain, R. K.; Bawendi, M. G.; et al. Shortwave infrared fluorescence imaging with the clinically approved near-infrared dye indocyanine green. *Proc. Natl. Acad. Sci. U.S.A.* **2018**, *115*, 4465−4470.

(50) Hu, Z.; Fang, C.; Li, B.; Zhang, Z.; Cao, C.; Cai, M.; Su, S.; Sun, X.; Shi, X.; Li, C.; et al. First-in-human liver-tumour surgery guided by multispectral fluorescence imaging in the visible and near-infrared-I/II windows. *Nat. Biomed. Eng.* **2019**, *4*, 259−271.

(51) McHugh, K.; Jing, L.; Severt, S. Y.; Cruz, M.; Sarmadi, M.; Jayawardena, H. S. N.; Perkinson, C. F.; Larusson, F.; Rose, S.; Tomasic, S.; et al. Biocompatible near-infrared quantum dots delivered to the skin by microneedle patches record vaccination. *Sci. Transl. Med.* **2019**, *11*, No. eaay7162.